ACS APPLIED MATERIALS & INTERFACES

Research Article

Cite This: ACS Appl. Mater. Interfaces 2019, 11, 2448−2458

www.acsami.org

New Cell-Penetrating Peptide (KRP) with Multiple Physicochemical Properties Endows Doxorubicin with Tumor Targeting and Improves Its Therapeutic Index

Mei Yu,[†] Xiaolong Li,[†] Xiaofeng Huang,[†] Jing Zhang,[†] Yan Zhang,[‡] and Hua Wang*[,†]

[†]Department of Oral and Maxillofacial Surgery, Guanghua School of Stomatology, Hospital of Stomatology and Guangdong Provincial Key Laboratory of Stomatology, SunYat-sen University, Guangzhou 510055, China

[‡]Laboratory of Cancer and Stem Cell Biology, Key Laboratory of Gene Engineering of the Ministry of Education, State Key Laboratory of Biocontrol, School of Life Sciences, Sun Yat-sen University, Guangzhou Higher Education Mega Center, Guangzhou 510006, China

Supporting Information

ABSTRACT: Cell-penetrating peptides (CPPs) are considered as promising drug carriers by virtue of their potent cell-penetrating capacity. However, lack of targetability still represents a bottleneck for their systemic administration. Here, we synthesized a lysine-rich CPP named KRP and developed a tumor-targeted drug delivery system (DDS) by linking KRP and doxorubicin (DOX) with stable covalent bonds (thioether bond and amide bond). Through in vitro and in vivo tests, we confirmed that the multiple physicochemical properties of KRP endow KRP-DOX with multiple synergistic functions, including good biocompatibility and biodistribution, selective accumulation in tumor tissues, inclination to remain in tumor tissues and be internalized by tumor cells; stable covalent bonds prevent free DOX release from KRP-DOX in blood stream, shield normal tissues from the toxic effect of DOX, and lead to the majority of DOX delivery into tumor cells by KRP; lysosome escape of KRP-DOX ensures its tumor-killing effect. In addition, the simple chemical composition and modification reduce the risk of immunogenicity and metabolite toxicity. Our study provides a simple, safe, and efficient platform for tumor-targeted DDS.

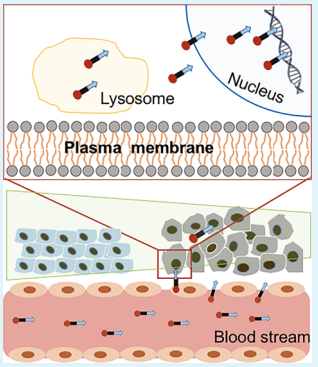

KEYWORDS: *cell-penetrating peptides (CPPs), drug delivery system (DDS), KRP-DOX, tumor targeting*

1. INTRODUCTION

To improve the therapeutic index (i.e., efficacy and safety) of antitumor drugs, it is necessary to endow them with multiple properties, such as good biocompatibility, stability in blood stream, tumor targeting, inclination to remain in tumor tissues and be internalized by tumor cells, etc. For this purpose, tumor-targeted drug delivery system (DDS) attracted wide attention in recent decades. After systemic administration, DDS needs to go through at least five cascade steps: circulation in the blood compartments, accumulation and penetration in tumors, cellular internalization, followed by intracellular drug release, which is named the CAPIR cascade.[1] It is important to take into account the majority of the above-mentioned barriers in tumor-targeted DDS design.[2] Among many nanocarriers, cell-penetrating peptides (CPPs) exhibit superiority for their cell-penetrating capacity. Since the first CPP, i.e., the trans-activator of transcription (TAT) protein of HIV-1 was discovered in 1988,[3] studies on CPPs have subverted the notion that hydrophilic macromolecules could not penetrate biofilms[4] and confirmed potent capacity of CPPs to deliver a large number of different types and sizes of substances into cells (including small molecules, plasmid DNA, peptides, proteins, nanoparticles, liposomes, viruses, quantum dots, etc.).[5−16] However, lack of targetability restricted systemic administration of CPPs. The common strategies to develop targeted CPP−drug conjugates are as follows: complement a ligand (with high affinity or specificity to the target tissues/cells), such as tumor-targeting peptides, antibodies, and homing peptides,[17−24] to CPP−drug conjugates; take advantage of the special microenvironment of target tissues (such as pH-sensitivity, oxidative or reducing environment, high expression of MMP, GSH, etc.) to trigger the cleavage of the junction for stimulus-responsive release.[25−29] To date, CPP−drug conjugates still stay at the door of clinical application. The reasons involve the following five points: (1) complex composition, excessive chemical modification increasing the instability, immunogenicity, and antigenicity of DDS. So, DDS is more susceptible to enzymatic hydrolysis in circulating blood or phagocytosis by the mononuclear phagocytic system.[30−32] (2) Excipients degrade into toxic products and damage normal tissues. (3) Individual differences of antigen or ligand expression on tumor cells also lead to unstable efficacy of antibodies in DDS.[33] (4) After the components of DDS are covalently linked, the physiochemical properties of some

Received: November 30, 2018
Accepted: December 21, 2018
Published: December 21, 2018

DOI: 10.1021/acsami.8b21027
ACS Appl. Mater. Interfaces 2019, 11, 2448−2458

Table 1. Physicochemical Properties of KRP

amino acid sequence	SSKEKKKGKKRKKKRREREGQKEGGRRKEKRKEKKRKEGGREGRKEGRKSADHPS
molecular weight	6402.35
pI (isoelectric point)	11.5
net charge at pH 7.0	+18.1
hydrophilic residue ratio	80%

Scheme 1. Design of KRP-DOX That Can Optimize the Biodistribution of DOX, Selectively Accumulate in Tumors, and Be Efficiently Internalized by Tumor Cells, Exerting an Antitumor Mechanism after Lysosome Escape

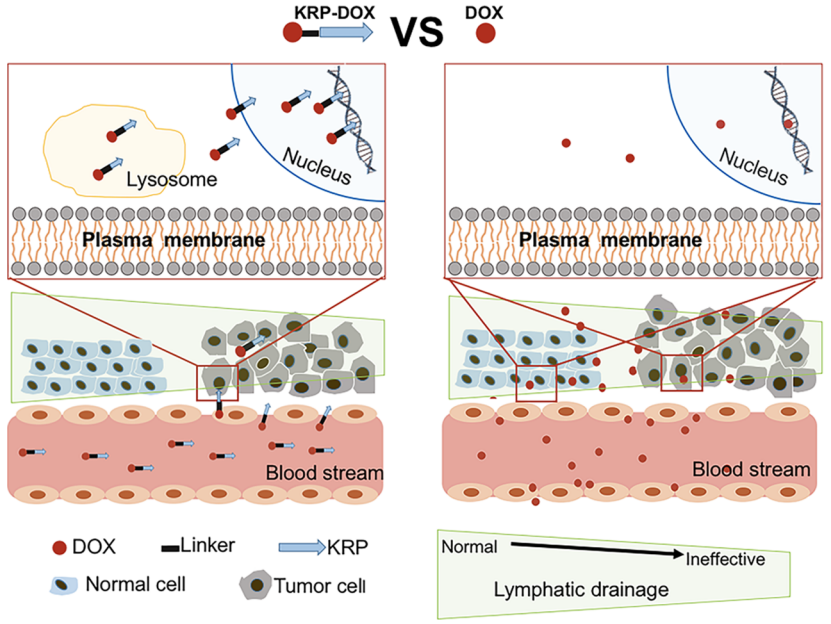

components are changed, thus resulting in no synergistic effect. (5) DDS failed to escape from lysosomes after being internalized by cells.

KRP is a lysine-rich CPP with multiple physicochemical properties (Table 1), which was discovered in our previous research.[34]

On the basis of the following reasons, we speculate that it is possible to construct a tumor-targeting DDS by linking KRP to DOX through stable covalent bonds: (1) The hydrophilic residue ratio of KRP is 80%, which endows KRP with hydrophilicity. Therefore, after intravenous administration, KRP circulates and remains in the blood stream rather than accumulating and precipitating. (2) The molar mass of KRP is more than that of DOX. KRP is not easy to flow out through the gap of normal vascular endothelial cells, i.e., not inclined to reach normal tissues. The stable covalent bond prevents the antitumor drugs' release from KRP in the blood stream and shields normal tissues from the toxic effects. (3) Unlike the common CPPs used as drug carriers (such as TAT, pAnt, MAP, R8, VP22, etc.), which are generally composed of less than 20 amino acid residues,[35] KRP is a 54 amino acid polypeptide. So, KRP is more likely to utilize the enhanced permeation and retention (EPR) effect[36−38] to achieve passive tumor targeting and remain in a solid tumor with long retention. (4) KRP is a basic polypeptide. Due to the vigorous metabolism, the local microenvironment of solid malignant tumors is mostly acidic. Basic KRP tends to accumulate in acidic microenvironment of tumors.[39,40] (5) KRP possesses 18 positive charges under physiological conditions and is apt to adsorb to the negative charges of heparin D sulfate in the membrane of tumor cells through electrostatic interaction. (6) Taking advantage of the potent cell-penetrating ability, KRP can load antitumor drugs into tumor cells efficiently. (7) There are two nucleus localization sequences[41] in KRP (KKRK), which may lead the drug to the nucleus. In a word, KRP-DOX may modify the bio-distribution model of DOX, i.e., replace the simple diffusion[2,42−44] into many organs with selective accumulation in solid tumors by the EPR effect (Scheme 1).

2. EXPERIMENTAL SECTION

2.1. Materials. Human osteosarcoma cell line (MG63) and Human umbilical vein endothelial cells (HUVECs) were purchased from ATCC (Manassas, VA). Cell culture media (DMEM, F12) was purchased from Sigma-Aldrich (St. Louis, MO). Fetal bovine serum (FBS) was purchased from Novagen (Madison, Wisconsin). Cell Counting Assay Kit-8 (CCK-8) was purchased from Dojindo Laboratory (Kumamoto, Japan). LysoTracker Green and 4′,6-diamidine-2′-phenylindole dihydrochloride (DAPI) were purchased from ThermoFisher Scientific. Doxorubicin (DOX) and Doxorubicin hydrochloride (DOX-HCL) were purchased from Hisun Pharmaceutical Co. (Zhejiang, China). All other chemicals were reagent grade.

2.2. Synthesis of KRP, KRP-DOX, and FITC-KRP-DOX. KRP were synthesized according to standard Fmoc solid-phase peptide synthesis (SPPS) methods,[45] conjugated to DOX through a c-terminal 3-maleimidopropionic acid "linker", conjugated to FITC through an N-terminal 6-aminohexanoic acid "linker" as described.[46] KRP, KRP-DOX, and FITC-KRP-DOX were confirmed and purified by reversed phase high-performance liquid chromatography electrospray ionization mass spectrometry (RP-HPLC/ESI MS).[47,48]

2.3. Cell Culture. MG63 cells were cultivated in DF (DMEM/F12) + 5% FBS. HUVECs were cultivated in DMEM + 10% FBS. Cell

DOI: 10.1021/acsami.8b21027
ACS Appl. Mater. Interfaces 2019, 11, 2448−2458

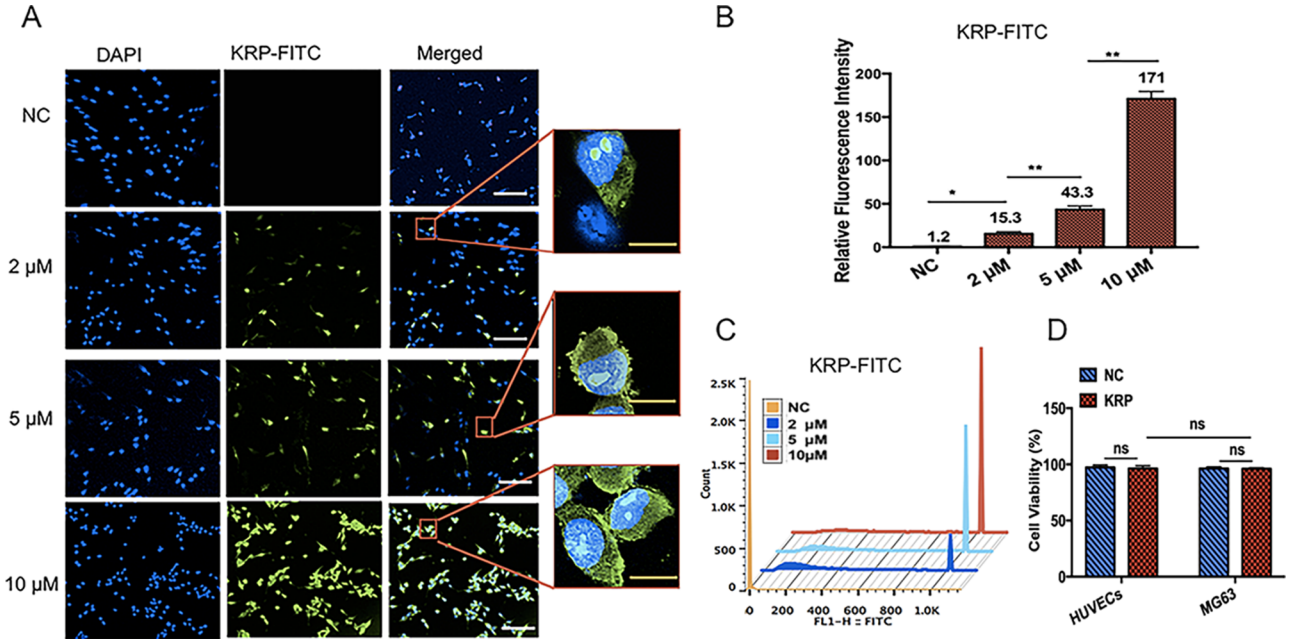

Figure 1. Characteristics of KRP. (A) By CLSM, FITC-KRP was observed to be internalized by MG63 cells in a dose-dependent manner. (B) By the image processing software ImageJ, the relative fluorescence density of FITC-KRP at various concentrations confirmed the dose-dependent manner of cellular internalization of KRP. (C) Flow cytometry further confirmed the above-mentioned result. (D) By Cell counting assay (CCK-8), KRP showed little cytotoxicity on MG63 cells and HUVECs at 10 μM concentration after 24 h of administration. The nuclei were stained with DAPI. White scale bars = 100 μm; yellow scale bars =10 μm.

culture was always performed at 37 °C in 5% CO_2 and 100% relative humidity.

2.4. Cellular Uptake Study. *2.4.1. Confocal Laser Scanning Microscopy (CLSM).* MG63 cells were seeded on a coverslip in a 6-well plate at the density of 5×10^4 cells/mL and cultured for 24 h. Then, the cells were washed with phosphate buffered saline (PBS) and incubated with different concentrations of FITC-KRP (2, 5, and 10 μM) for 1 h (saline as negative control/NC). The same method is used to prepare MG63 cells for evaluating the cellular uptake of KRP-DOX and DOX-HCL. The treated cells were rinsed in PBS for 5 min. Coverslip slides were used with ProlongGold Anti-Fade Reagent (with DAPI for nucleus staining). CLSM was used to observe the fluorescence. Images were acquired with a resolution of 1024 × 1024 pixels using a 5× and an oil-immersion 63× objective. The wavelength of the argon-ion laser was set at 488 nm; fluorescence emission was observed at 520−530 nm for FITC and 570−600 nm for DOX. The relative fluorescence intensity of each slice was calculated by image processing software ImageJ, as described in our previous study.[34]

2.4.2. Flow Cytometry. For quantitative analysis, the treated cells were washed with cold PBS, trypsinized, and harvested by centrifugation at 1000 rpm for 5 min. The cells were resuspended in 200 μL of PBS and analyzed by flow cytometry (BD). The excitation wavelength was set at 488 nm; fluorescence emission was at 520−530 nm for FITC and 570−600 nm for DOX. Images were analyzed using image-analysis software Flow Jo vX.0.7.

2.5. Cytotoxicity Assay. The effects of KRP, KRP-DOX, and DOX on cell proliferation were studied with MG63 cells and HUVECs by the CCK-8 assay. The cells (4×10^3 cells per well) were seeded in 96-well plates and cultured for 24 h. Drugs at various concentrations were added to the culture medium. Twenty-four hours later, 10 μL of CCK-8 solution was added to each well and the cells were incubated for another 2 h. The absorbance values were then measured at 450 nm using a VICTOR X5 Multilabel plate reader (PerkinElmer, Inc., Singapore). Cell viability (%) was expressed by the following equation: Cell viability (%) = $(A_{sample} - A_{baseline})/(A_{control} - A_{blank}) \times 100\%$. A_{sample} stood for absorbance of the experimental well (containing cells, medium, CCK-8 solution, and drug solution); $A_{baseline}$ stood for absorbance of the baseline well (containing medium, CCK-8 solution, and drug solution; no cells); $A_{control}$ stood for absorbance of the control well (containing cells, medium, and CCK-8 solution; no drug); and A_{blank} stood for the absorbance of the blank well (containing medium, CCK-8 solution, no cells, drugs).

2.6. Lysosome Colocalization. MG63 cells were seeded on a coverslip in a 6-well plate at the density of 5×10^4 cells/mL. After 24 h, KRP-DOX (10 μM) was added to the culture medium. After 0.5 h (group 1) and 2 h (group 2), LysoTracker Green (50 nM) was added and incubated with the cells for 5 min for endosome/lysosome labeling. The incubation solution was removed and the cells were rinsed in PBS for 5 min and fixed with 4% paraformaldehyde (PFA) for 15 min. CLSM was used to observe the fluorescence, as previously mentioned.

2.7. Stability of KRP-DOX in MG63 Cells. MG63 cells were seeded on a coverslip in a six-well plate at the density of 5×10^4 cells/mL and cultured for 24 h. Then, the cells were washed with PBS and incubated with FITC-KRP-DOX (10 μM) for 2 h. The treated cells were rinsed in PBS for 5 min and fixed with 4% PFA for 15 min. Fluorescence Images were acquired and observed, as mentioned above.

2.8. In Vivo Experiments. *2.8.1. Animal Preparation.* All animal experiments were carried out in accordance with guidelines approved by the Animal Ethical and Welfare Committee of Sun Yat-sen University (Guangzhou, Guangdong, China). A total of 5×10^6 MG63 cells in 100 μL of PBS was injected subcutaneously in the right flanks of 5 week old male BALB/c node mice. When the xenograft tumors approached 8 mm diameter, the tumor-bearing mice were randomly divided into three groups: The mice in DOX group received DOX-HCL administration (at a dose equivalent to 5 mg/kg free DOX) daily via tail vein injection. The KRP-DOX group received KRP-DOX administration (at a dose equivalent to 5 mg/kg free DOX) daily via tail vein injection. DOX-HCL and KRP-DOX were dissolved in 100 μL of saline. The control group received 100 μL of saline administration via tail vein injection daily. The administration process lasted for 1 week.

2.8.2. DOX Release Assessment. Before the end of the animal experiment, the blood samples (200 μL) were collected through ophthalmectomy at predefined time intervals (5, 30 min, 1, 2, 6, 12, 24, and 48 h after drug administration). The collected samples were

DOI: 10.1021/acsami.8b21027
ACS Appl. Mater. Interfaces 2019, 11, 2448−2458

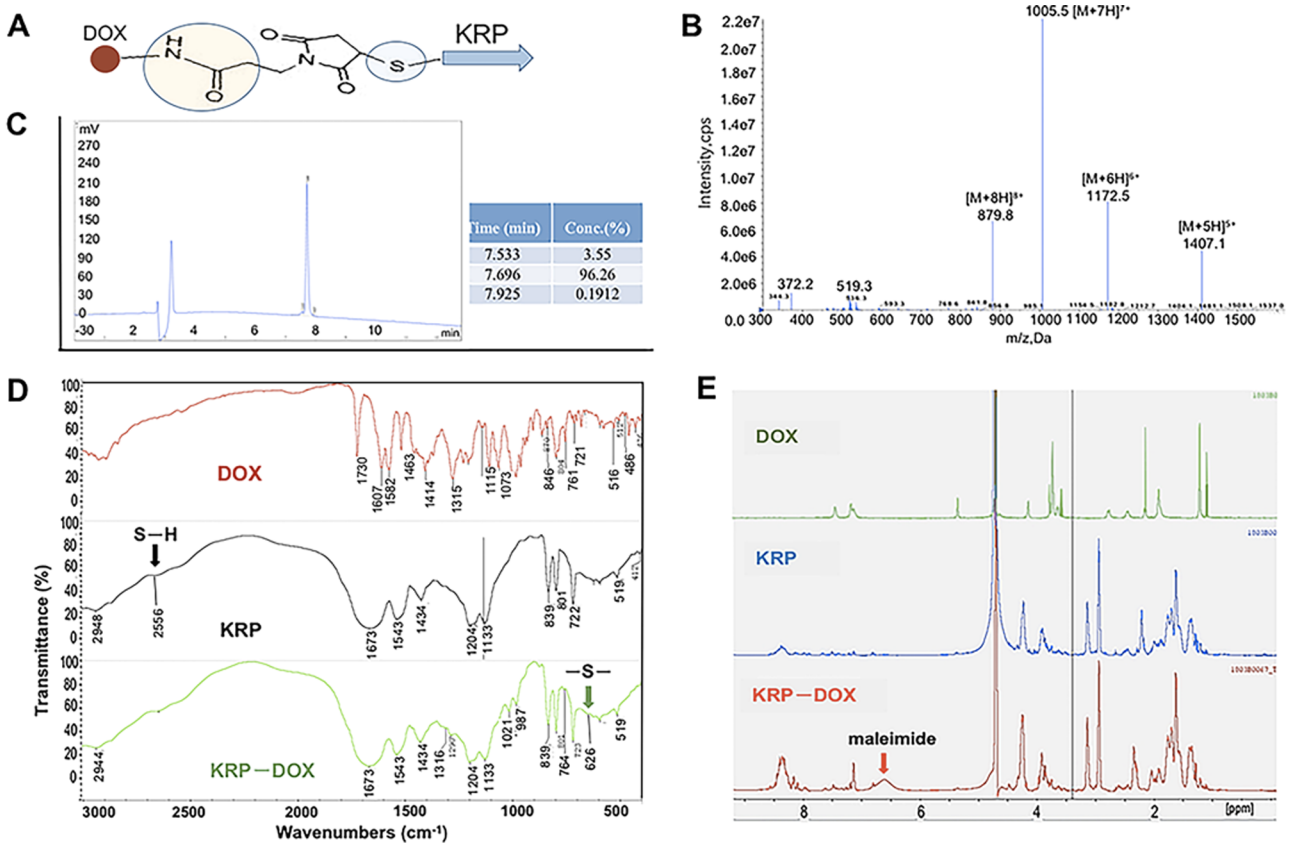

Figure 2. Design and synthesis of KRP-DOX. (A) Three components of KRP-DOX, maleimidopropionic acid acting as a linker to link the amino group of DOX with amide bond (in the yellow ellipse) and the cysteine residue of KRP with thioether bond (in the blue ellipse). (B) Mass spectrum of KRP-DOX. According to the mass-to-charge ratio, the molecular weight of the synthesized compound was in the range of 7035−7038, which is consistent with that of KRP-DOX. (C) HPLC assay showed that the purity of KRP-DOX was 96.26%. (D) FTIR spectra showed the typical S−H bond at 2600−2500 cm^{-1} (black arrow, in KRP) and −S− bond at 640−600 cm^{-1} (blue arrow, in KRP-DOX), which indicated successful connection of KRP and DOX via a thioether bond. (E) The ^{1}H NMR spectrum of KRP-DOX indicated the presence of the maleimide group by its characteristic peak at 6.7 ppm. The results indicated the successful reaction of the thiol group of KRP with the linker (maleimide group).

centrifuged at 12 000 rpm for 10 min, and the supernatant were extracted and stored at −80 °C. The concentration of free DOX in plasma samples at different times after drug administration was determined by liquid chromatography tandem mass spectrometry (LC-MS/MS), as previously described,[49] using daunorubicin as internal standard (IS) (Supporting Information).

2.8.3. In Vivo Imaging and Biodistribution Analysis. In vivo imaging system/IVIS (PerkinElmer) was used to take the ex vivo images of tumor-bearing mice (including DOX-HCL group and KRP-DOX group, with saline group as control; the grouping method is as mentioned before) at predefined time intervals (1, 6, 12, 24, and 48 h after drug administration) with excitation wavelength from 475−485 nm and emission wavelength from 575−585 nm. The heart, liver, spleen, lung, kidney, and tumor were collected from each humanely killed mouse 6 h after injection. The fluorescence intensity in all organs was analyzed by IVIS spectrum. At last, the frozen sections (10 μm) of the tumors, hearts, and livers were stained with DAPI. The fluorescence of each section was analyzed by CLSM according to DOX excitation (475−485 nm) and emission wavelength (575−585 nm).

2.9. Statistical Analyses. Statistical analyses were performed by the software GraphPad Prism (version 7.0a). Two-tailed unpaired Student's *t*-test was used for statistical analysis when a pair of conditions was compared. The analysis for each sample was repeated at least three times. Asterisks denote statistical significance ($*P < 0.05$; $**P < 0.01$; $***P < 0.001$). The data are reported as mean ± SD.

3. RESULTS AND DISCUSSION

3.1. Design and Synthesis of KRP-DOX. *3.1.1. Characteristics of KRP.* KRP and FITC-labeled KRP (FITC-KRP) have been synthesized in our previous study. In this study, KRP and FITC-KRP were confirmed and purity analyzed by RP-HPLC/ESI MS (Figures S1 and S2). The cellular internalization tendency of KRP at various concentrations was assessed to decide a rational concentration for subsequent studies. As exhibited in Figure 1A, by CLSM, FITC-KRP was detected with green fluorescence of FITC (with excitation wavelength from 490−495 nm and emission wavelength from 520−530 nm). The cellular nuclei were stained with DAPI for blue fluorescence (with an excitation wavelength of 358 nm and an emission wavelength of 461 nm). FITC-KRP was internalized by MG63 cells in a dose-dependent manner. FITC-KRP appeared in almost all MG63 cells at 10 μM concentration after 2 h of administration. As exhibited in Figure S3, FITC-KRP was observed to be internalized by HUVECs in a dose-dependent manner too. By the image processing software ImageJ, the relative fluorescence density was calculated and demonstrated the concentration-dependent cell internalization of KRP (Figure 1B). Flow cytometry further confirmed this result (Figure 1C). To study the effect of KRP on the proliferation of both cancer cells and normal cells, cell counting assay (CCK-8) was performed on MG63

DOI: 10.1021/acsami.8b21027
ACS Appl. Mater. Interfaces 2019, 11, 2448−2458

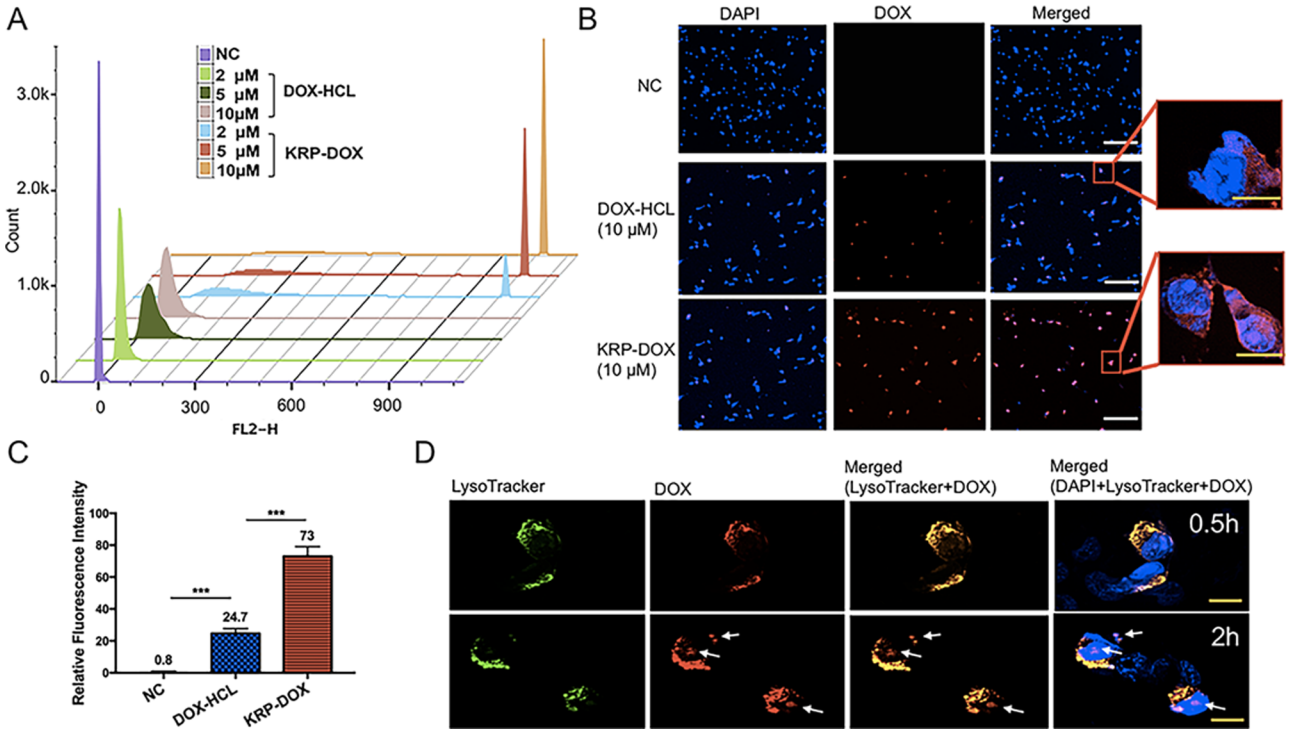

Figure 3. Characteristics of KRP-DOX. (A) Flow cytometry assay showed that the affinity of KRP-DOX to MG63 cells is more than 3 times stronger than that of DOX-HCL at the same concentration, after 2 h of drug administration. (B, C) At the concentration of 10 μM, by CLSM, a majority of MG63 cells in KRP-DOX group/minority of MG63 cells in DOX-HCL group exhibited the red fluorescence of DOX. Relative fluorescence intensity by ImageJ confirmed this result. (D) Red fluorescence of DOX from KRP-DOX colocalized with the green fluorescently labeled lysosomes in MG63 cells (emerged as yellow fluorescence) after incubation for 0.5 h. After incubation for 2 h, the red fluorescence began to separate from the green fluorescently labeled lysosomes and appeared in both cytoplasm and nuclei of MG63 cells (white arrow). The nuclei were stained with DAPI. White scale bars = 100 μm; yellow scale bars = 10 μm.

cells and HUVECs. As shown in Figure 1D, KRP showed little cytotoxicity on both kinds of cells at 10 μM concentration after 24 h of administration.

3.1.2. Design of KRP-DOX. On the basis of the potent cell-penetrating capacity and nontoxic property of KRP, combined with its physicochemical properties, we designed a tumor-targeted DDS (KRP-DOX) that contains only three components: (1) a new cell-penetrating peptide (KRP). (2) a model chemotherapy drug (doxorubicin, DOX) The clinical application of DOX is restricted for dose-dependent myelosuppression, a significant incidence of irreversible cardiotoxicity, and the development of drug resistance. (3) a linker: maleimidopropionic acid, which links the amino group of DOX with amide bond and the cysteine residue of KRP with thioether bond (Figure 2A).

3.1.3. Synthesis of KRP-DOX. KRP-DOX was synthesized by Fmoc Chemistry (China Peptide Company, Jiangsu, China), as described in the literature,[50] confirmed with purity analysis by RP-HPLC/ESI MS. Maleimidopropionic acid acted as a linker to link the amino group of DOX with amide bond (in the yellow ellipse) and the cysteine residue of KRP with thioether bond (in the blue ellipse) (Figure 2A). The molecular weight of KRP-DOX is composed of KRP (7031), DOX (543.5), and linker. According to the mass-to-charge ratio, the molecular weight of the synthesized compound was in the range of 7035−7038, which is consistent with that of KRP-DOX (Figure 2B). HPLC assay showed that the purity of KRP-DOX was 96.26% (Figure 2C). The structure was verified by Fourier transform infrared spectroscopy (FTIR) and ^{1}H NMR spectroscopy (400 MHz, DMSO-d_6). FTIR spectra showed the typical S−H bond at 2600−2500 cm^{-1} (black arrow, in KRP) and −S− bond at 640−600 cm^{-1} (blue arrow, in KRP-DOX), which indicated successful connection of KRP and DOX via thioether bond(Figure 2D). The ^{1}H NMR spectrum of KRP-DOX indicated the presence of the maleimide group by its characteristic peak at 6.7 ppm, whereas that of KRP did not show. The results indicated the successful reaction of the thiol group of KRP with the linker (maleimide group) (Figure 2E).

3.2. Characteristics of KRP-DOX. To determine whether KRP can efficiently transport DOX into tumor cells, we performed a series of experiments.

3.2.1. Tumor Cell Affinity of KRP-DOX. Tumor cell affinity is the first factor affecting cellular uptake of KRP-DOX. Taking advantage of self-fluorescence from DOX, by flow cytometry, MG63 cells combined with both KRP-DOX and DOX-HCL exhibited red fluorescence. MG63 cells which received no drug application served as negative control (NC). Figure 3A shows that at the same concentration, after 2 h of drug administration, the fluorescence intensity of MG63 cells in KRP-DOX group is more than 3 times higher than that in DOX group; both of them are concentration dependent. That means, the cell affinity of KRP-DOX to MG63 is obviously stronger than that of DOX-HCL.

3.2.2. Cellular Uptake Tendency of KRP-DOX. Because flow cytometry cannot distinguish membrane-bound drugs from drugs entering cells, the internalization tendency of KRP-DOX and DOX-HCL to MG63 cells was compared further by CLSM. As demonstrated in Figure 3B, at 10 μM concentration, after 2 h of administration, the red fluorescence of DOX can be

DOI: 10.1021/acsami.8b21027
ACS Appl. Mater. Interfaces 2019, 11, 2448−2458

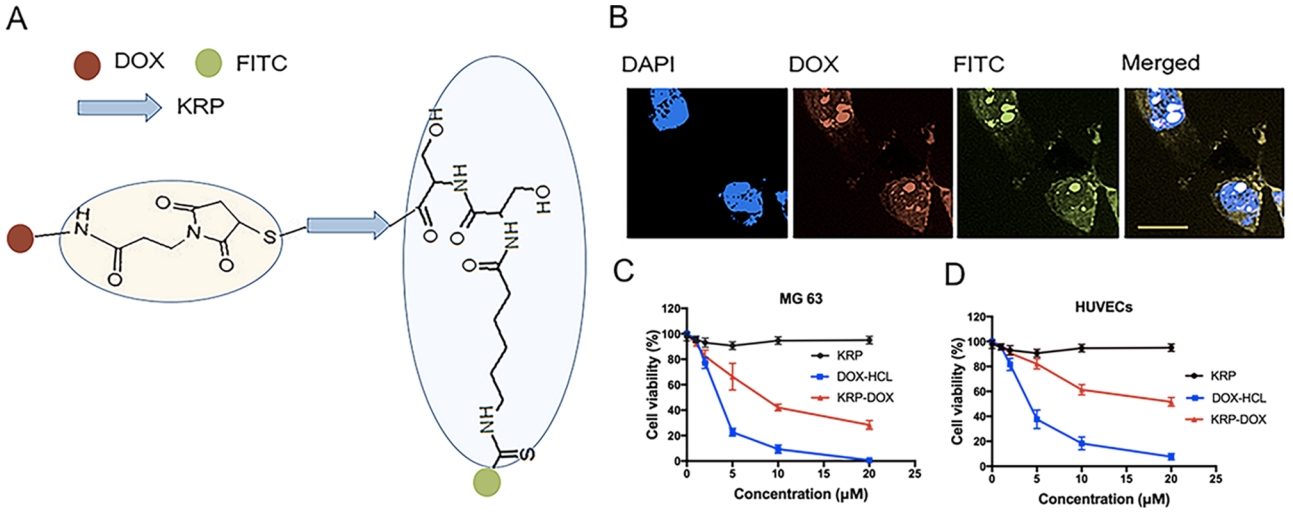

Figure 4. Stability and cytotoxicity of KRP-DOX. (A) Design of FITC-KRP-DOX: Maleimidopropionic acid (in the yellow ellipse) and 6-aminocaproic acid/Acp (in the blue ellipse) served as linkers (B) By CLSM (63× oil-immersion objective), the distribution of green fluorescence (FITC) and red fluorescence (DOX) from FITC-KRP-DOX in MG63 cells was consistent, both of them appeared in cytoplasm and nuclei after 2 h of administration. (C, D) DOX-HCL showed stronger cytotoxicity than KRP-DOX on MG63 cells and HUVECs at the same concentration. The nuclei were stained with DAPI. Yellow scale bar = 10 μm.

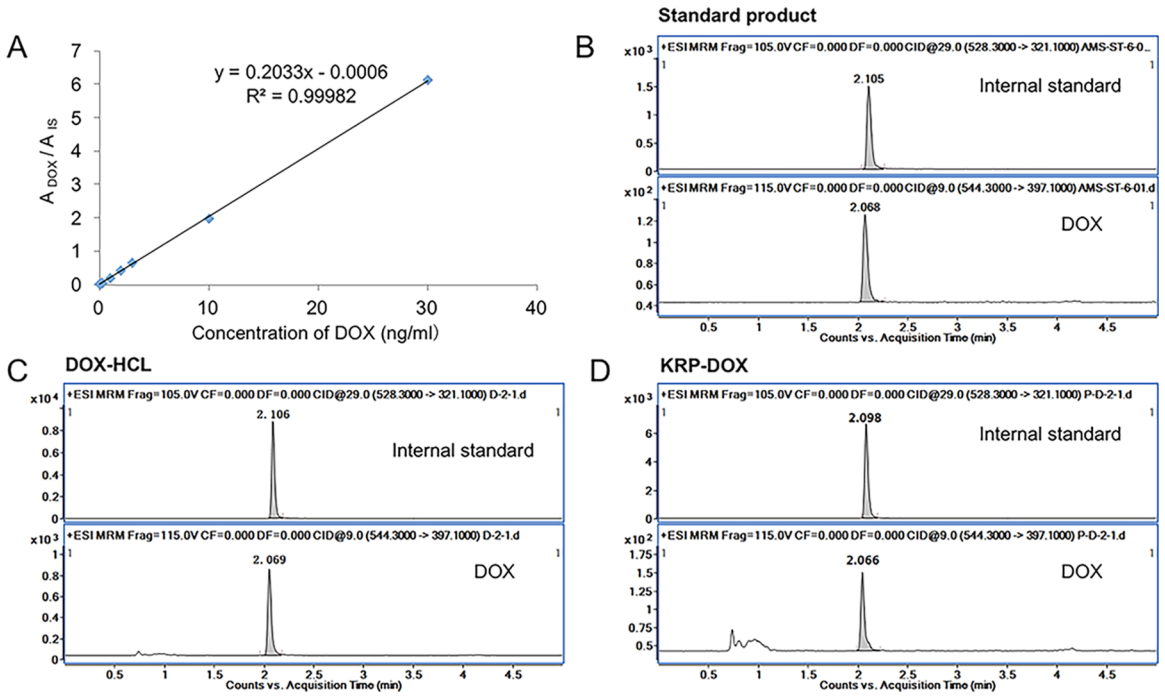

Figure 5. DOX release from KRP-DOX in the blood stream by LC-MS/MS analysis. (A) Using daunorubicin as internal standard (IS), the calibration curve showed good linearity with a regression coefficient of 0.99982. The ratio of the doxorubicin peak area to the daunorubicin peak area is the ordinate (A_{DOX}/A_{IS}) (B–D) Counts vs acquisition time (min) of DOX from standard product, DOX-HCL, and KRP-DOX, respectively, by HPLC.

observed in almost all MG63 cells in KRP-DOX group and in only about 1/3 of MG63 cells in DOX-HCL group. From a 63× oil-immersion objective of CLSM, red fluorescence of DOX was located in cytoplasm as well as nuclei in MG63 cells of both groups. To further confirm this result, the relative fluorescence density of both groups was calculated and compared by the image processing software ImageJ (Figure 3C).

3.2.3. Endolysosome Escape of KRP-DOX. Considering that different CPPs are taken up by cells in different way and different concentrations of peptide and the presence of the load may also alter the transport pathway, we tried to reveal the cellular uptake pathway and distribution of KRP-DOX in MG63 cells. Lysosome colocalization experiment was performed with LysoTracker Green (with an excitation wavelength from 490–495 nm and an emission wavelength from 520–530 nm). As exhibited in Figure 3D, red fluorescence of DOX from KRP-DOX colocalized with the green fluorescently labeled lysosomes in MG63 cells (emerged as yellow fluorescence) after incubation for 0.5 h. After

DOI: 10.1021/acsami.8b21027
ACS Appl. Mater. Interfaces 2019, 11, 2448–2458

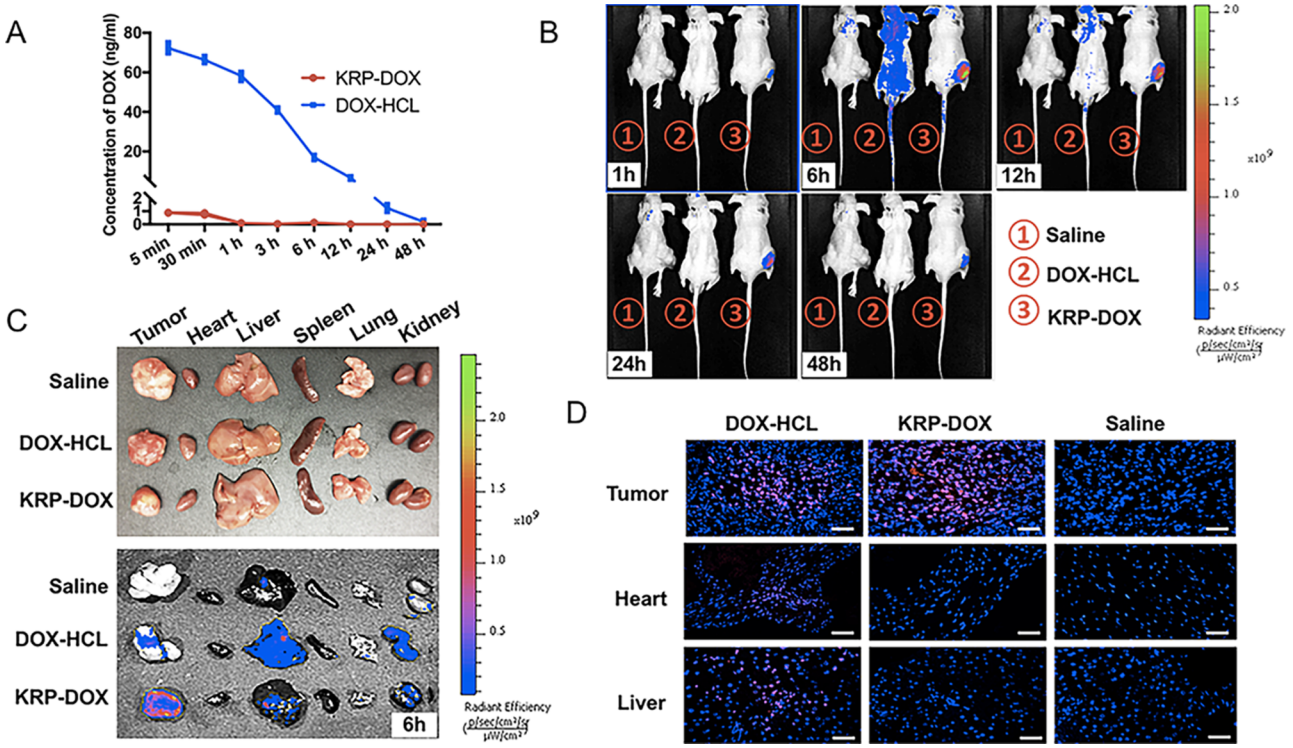

Figure 6. Stability of KRP-DOX in blood stream and biodistribution of KRP-DOX in vivo. (A) By LC-MS/MS, from 5 min to 48 h after intravenous administration of KRP-DOX, almost no free doxorubicin was detected in the blood stream. (B) By IVIS, KRP-DOX selectively accumulated in the tumor area after 1 h of administration; after 6 h of KRP-DOX administration, the fluorescence intensity in the tumor reached the highest level; after 48 h of KRP-DOX administration, the tumor area still showed fluorescence. Correspondingly, DOX-HCL dispersed and was excreted by liver and kidney metabolism. Twelve to twenty-four hours after DOX-HCL administration, the fluorescence of DOX disappeared in mice. (C) By IVIS, after 6 h of drug administration, KRP-DOX was mainly concentrated in tumor while DOX-HCL was dispersed in various organs, especially in liver and kidneys. (D) By CLSM, frozen sections exhibited that after 6 h of drug administration, red fluorescence of DOX was observed in tumor cells, cardiomyocytes, and hepatocytes of DOX-HCL group; red fluorescence was observed in tumor cells but not in cardiomyocytes and hepatocytes of KRP-DOX group. The nuclei were stained with DAPI. White scale bars = 50 μm.

incubation for 2 h, the red fluorescence began to separate from the green fluorescently labeled lysosomes and appeared in both cytoplasm and nuclei of MG63 cells. Although the entry mechanism is not entirely understood, our study suggested that KRP-DOX could enter MG63 cells by endocytosis and escape from the endolysosome into the cytoplasm and the nuclei. One proposed mechanism with which to disrupt lysosomes is the proton sponge effect, whereby nanoparticles with cationic surface groups induce osmotic lysis upon endosome acidification.[51]

3.2.4. Stability of KRP-DOX in Endolysosome. To further explore whether the entire KRP-DOX escaped from endolysosome or only the free DOX escaped from endolysosome after KRP being hydrolyzed, we labeled the KRP end of KRP-DOX with fluorescein FITC. FITC-KRP-DOX was synthesized by Fmoc chemistry and confirmed with purity analysis as mentioned above (Figure S4A,B). The 6-aminocaproic acid (Acp) served as a linker (Figure 4A). By CLSM (63× oil-immersion objective), we observed that the distribution of green fluorescence (FITC) and red fluorescence (DOX) in MG63 cells was consistent (Figure 4B); both appeared in cytoplasm and nuclei after 2 h of administration. This result can indirectly confirm that FITC-KRP-DOX remains intact in MG63 cells and acts as a whole.

3.2.5. Cytotoxicity of KRP-DOX. Finally, we compared the cytotoxicity of DOX-HCL and KRP-DOX on MG63 and HUVECs by CCK-8 assay. As revealed in Figure 4C, after a 24 h treatment with DOX-HCL and KRP-DOX at various concentrations, the viability of MG63 cells and HUVECs decreased in a dose-dependent manner. IC50 of DOX-HCL (MG63 cells/3.05 μM; HUVECs/4.15 μM) is less than that of KRP-DOX (MG63 cells/7.41 μM; HUVECs/19.44 μM).

3.3. In Vivo Experiment. *3.3.1. Free DOX Released by KRP-DOX and DOX-HCL in Circulating Blood.* To investigate whether KRP is rapidly degraded by serum protein and then release DOX, the amounts of DOX in serum were detected at different times by LC-MS/MS. Using daunorubicin as internal standard, the calibration curve showed good linearity with a regression coefficient of 0.99982 (Figure 5). As demonstrated in Figure 6A, less than 1 ng of DOX was detected 5 min after intravenous administration of KRP-DOX via tail vein injection; from 30 min to 48 h after intravenous administration, no free DOX was detected in the blood stream. This feature, on one hand, can shield the normal tissues from the direct toxicity of DOX, and on the other hand, also prevent released DOX from dispersing in the organs and resulting in undesirable toxic effects.

3.3.2. Biodistribution of KRP-DOX. The biodistribution of KRP-DOX and DOX-HCL in mice with xenograft osteosarcoma after tail vein injection was observed with red fluorescence of DOX by IVIS. As demonstrated in Figure 6B, KRP-DOX selectively accumulated in the tumor area after 1 h of KRP-DOX administration; after 6 h of KRP-DOX administration, the fluorescence intensity in tumor reached the highest level; after 48 h of KRP-DOX administration, the tumor area still showed fluorescence, suggesting that the retention period of

DOI: 10.1021/acsami.8b21027
ACS Appl. Mater. Interfaces 2019, 11, 2448−2458

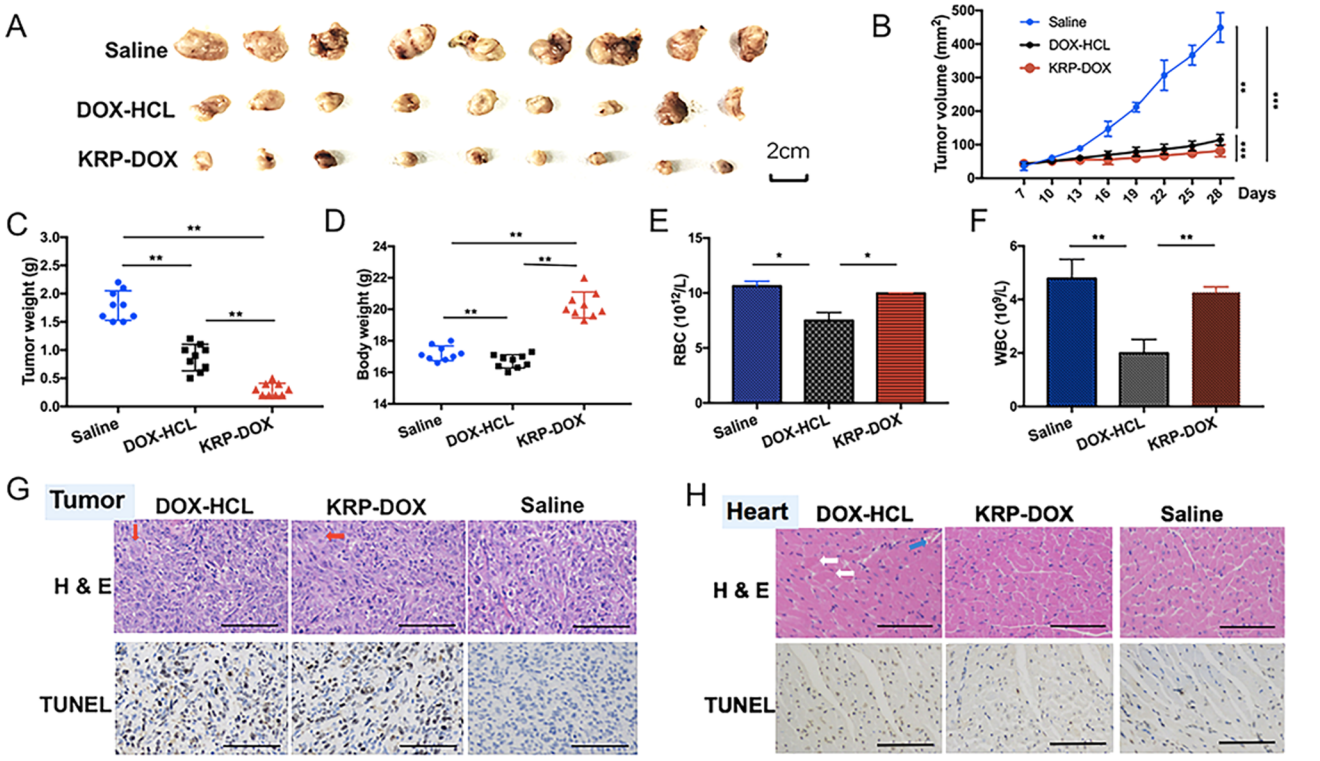

Figure 7. Antitumor efficacy of KRP-DOX. (A) Tumors in three groups (3 weeks after drug administration, 9 cases in each group). (B, C) The tumor volumes in saline group rapidly increased, whereas the growth of tumors was significantly suppressed after the treatment with DOX-HCL and KRP-DOX. (D) The mice in the DOX-HCL group were significantly thinner as compared with mice in KRP-DOX group. (E, F) The level of leukocytes and erythrocytes in mice blood showed that KRP-DOX significantly reduced the bone marrow inhibition of DOX. (G, H) By H&E staining, necrotic tumor tissues (red arrow, karyopyknosis, karyolysis) were observed in both DOX-HCL and KRP-DOX groups; in DOX-HCL group, myocardial cells were arranged in a disorder, wherein myocardial fibrosis (white arrow) and hemorrhage (blue arrow) were observed. By TUNEL staining (brown), compared with the control (Saline) group, the DOX-HCL and KRP-DOX group exhibited apparently stronger staining in the tumor regions; the TUNEL staining of myocardial cells in DOX-HCL group is thicker than that in KRP-DOX group. Black scale bars = 100 μm.

the KRP-DOX in mice osteosarcoma could reach 48 h. Correspondingly, DOX-HCL dispersed by simple diffusion after tail vein injection in mice with xenograft osteosarcoma and excreted by liver and kidney metabolism. Twelve to twenty-four hours after DOX-HCL administration, the fluorescence of DOX was not detected in mice, suggesting that the retention period of DOX-HCL in xenograft osteosarcoma mice was less than 24 h. To further observe the biodistribution of KRP-DOX in mice organs, we performed in vitro fluorescence imaging of mice organs by IVIS. Six hours after tail vein injection of saline, DOX, and KRP-DOX, we euthanized the mice and surgically removed the tumor, heart, liver, spleen, lungs, and kidneys for fluorescence imaging. As shown in Figure 6C, KRP-DOX was mainly concentrated in tumors whereas DOX-HCL was dispersed in various organs, especially in liver and kidneys, resulting in very low drug distribution in tumor areas. The frozen sections were observed by CLSM. Figure 6D demonstrated that red fluorescence was observed in tumor cells, as well as in cardiomyocytes and hepatocytes of DOX-HCL group; red fluorescence was observed in tumor cells but not in cardiomyocytes and hepatocytes of KRP-DOX group. The relative fluorescence intensity of DOX was qualified by image processing software ImageJ (Figure S5). The reasonable explanation for this result is enhanced permeability and retention (EPR) effect, which demonstrated the potential for heightened accumulation of macromolecules by extravasation through fenestrated blood vessels in tumors together with the lack of lymphatic drainage and opened several exciting avenues for site-specific localization of chemotherapeutics.[52] The ability of KRP-DOX to extravasate to solid tumor sites largely improved the safety and tolerability of DOX. The above-mentioned results gave us great expectation for the antitumor efficiency and safety of KRP-DOX.

3.3.3. Antitumor Efficacy of KRP-DOX. The antitumor efficacy of KRP-DOX was estimated in osteosarcoma xenograft mice. As shown in Figure 7A,B, the tumor volume of mice that received saline (control group) rapidly increased in 4 weeks whereas the growth of tumors was significantly suppressed after the treatment of DOX-HCL and KRP-DOX. The tumors were excised and weighed at the end of the experiment, demonstrating the same trend (Figure 7C). Meanwhile, the mice in the DOX-HCL group were significantly thinner as compared with mice in KRP-DOX group (Figure 7D). These results confirmed our prediction that the antitumor effect of KRP-DOX is stronger than that of DOX-HCL in vivo. Besides, the level of leukocyte erythrocyte in mice blood showed that KRP-DOX significantly reduced the bone marrow inhibition of DOX-HCL (Figure 7E,F).

3.3.4. Histological Analyses. To further characterize the antitumor efficacy in vivo at a pathological level, histological analyses were performed. By hematoxylin and eosin (H&E) staining, necrotic tumor tissues were observed in both DOX-HCL and KRP-DOX groups; in DOX-HCL group, myocardial

DOI: 10.1021/acsami.8b21027
ACS Appl. Mater. Interfaces 2019, 11, 2448−2458

cells were arranged in a disorder, wherein myocardial fibrosis and hemorrhage were observed. By TUNEL staining (brown), the level of apoptosis in tumor tissues was determined: compared with the control (saline) group, the DOX-HCL and KRP-DOX group exhibited apparently stronger staining in the tumor regions, demonstrating that cancer cells entered the apoptotic process. At the same time, it is consistent with our expectation that the TUNEL staining of myocardial cells in DOX-HCL group is thicker than that in KRP-DOX group. This shows that the damage by KRP-DOX to myocardium is obviously weaker than that by DOX (Figure 7G,H).

4. CONCLUSIONS

Our scientific hypothesis was verified by the in vivo and in vitro experiments. After being intravenously administered into the xenograft osteosarcoma mice, almost no free DOX was released by KRP-DOX in the circulating blood, so normal tissues were shielded from the direct toxic effects of DOX; KRP-DOX can modify the biodistribution model of the small molecule DOX, i.e., replace the simple diffusion into many organs with selective accumulation in solid tumors by the EPR effect since KRP-DOX has many positive charges, which can bind to tumor cells by electrostatic interaction with the negative charges on tumor cell membranes. KRP-DOX can be efficiently internalized by tumor cells and can escape from endolysosome. KRP-DOX can enter nuclei and exert a tumor-killing effect. Our research provides a simple, safe, and efficient platform for tumor-targeted DDS.

■ ASSOCIATED CONTENT

Supporting Information

The Supporting Information is available free of charge on the ACS Publications website at DOI: 10.1021/acsami.8b21027.

Mass spectrum and HPLC of KRP; mass spectrum and HPLC of FITC-KRP; cell internalization characteristics of KRP by HUVECs; mass spectrum and HPLC of FITC-KRP-DOX; relative fluorescence (DOX) intensity in tumor/heart/liver of saline, KRP-DOX and DOX-HCL groups (Figures S1−S5); FITC-KRP-DOX synthesis steps; DOX release assessment by LC-MS/MS (PDF)

■ AUTHOR INFORMATION

Corresponding Author

*E-mail: wanghua9@mail.sysu.edu.cn.

ORCID

Hua Wang: 0000-0002-1576-6151

Notes

The authors declare no competing financial interest.

■ ACKNOWLEDGMENTS

This work was supported by a grant from National Natural Science Foundation of China (grant no. 31371390), National High-tech R&D Program (863 Program) of Chinese Ministry of Science and Technology (No. 2014AA020702), and two Programs of Guangdong Science and Technology Department (Nos. 2016B030231001 and 2017B020230002). The funding source had no role in the study design, data collection, data analysis, data interpretation, and writing of this paper.

■ REFERENCES

(1) Sun, Q.; Zhou, Z.; Qiu, N.; Shen, Y. Rational Design of Cancer Nanomedicine: Nanoproperty Integration and Synchronization. *Adv. Mater.* **2017**, *29*, No. 1606628.

(2) Blanco, E.; Shen, H.; Ferrari, M. Principles of nanoparticle design for overcoming biological barriers to drug delivery. *Nat. Biotechnol.* **2015**, *33*, 941−951.

(3) Frankel, A. D.; Pabo, C. O. Cellular uptake of the tat protein from human immunodeficiency virus. *Cell* **1988**, *55*, 1189−1193.

(4) Sánchez-Navarro, M.; Teixido, M.; Giralt, E. Jumping Hurdles: Peptides Able To Overcome Biological Barriers. *Acc. Chem. Res.* **2017**, *50*, 1847−1854.

(5) Lewin, M.; Carlesso, N.; Tung, C. H.; Tang, X. W.; Cory, D.; Scadden, D. T.; Weissleder, R. Tat peptide-derivatized magnetic nanoparticles allow in vivo tracking and recovery of progenitor cells. *Nat. Biotechnol.* **2000**, *18*, 410−414.

(6) Huang, S.; Shao, K.; Liu, Y.; Kuang, Y.; Li, J.; An, S.; Guo, Y.; Ma, H.; Jiang, C. Tumor-targeting and microenvironment-responsive smart nanoparticles for combination therapy of antiangiogenesis and apoptosis. *ACS Nano* **2013**, *7*, 2860−2871.

(7) Rothbard, J. B.; Garlington, S.; Lin, Q.; Kirschberg, T.; Kreider, E.; McGrane, P. L.; Wender, P. A.; Khavari, P. A. Conjugation of arginine oligomers to cyclosporin A facilitates topical delivery and inhibition of inflammation. *Nat. Med.* **2000**, *6*, 1253−1257.

(8) Sangtani, A.; Petryayeva, E.; Wu, M.; Susumu, K.; Oh, E.; Huston, A. L.; Lasarte-Aragones, G.; Medintz, I. L.; Algar, W. R.; Delehanty, J. B. Intracellularly Actuated Quantum Dot-Peptide-Doxorubicin Nanobioconjugates for Controlled Drug Delivery via the Endocytic Pathway. *Bioconjugate Chem.* **2018**, *29*, 136−148.

(9) Tian, R.; Wang, H.; Niu, R.; Ding, D. Drug delivery with nanospherical supramolecular cell penetrating peptide-taxol conjugates containing a high drug loading. *J. Colloid Interface Sci.* **2015**, *453*, 15−20.

(10) Oh, E.; Delehanty, J. B.; Sapsford, K. E.; Susumu, K.; Goswami, R.; Blanco-Canosa, J. B.; Dawson, P. E.; Granek, J.; Shoff, M.; Zhang, Q.; Goering, P. L.; Huston, A.; Medintz, I. L. Cellular uptake and fate of PEGylated gold nanoparticles is dependent on both cell-penetration peptides and particle size. *ACS Nano* **2011**, *5*, 6434−6448.

(11) Fan, L. Q.; Du, G. X.; Li, P. F.; Li, M. W.; Sun, Y.; Zhao, L. M. Improved breast cancer cell-specific intracellular drug delivery and therapeutic efficacy by coupling decoration with cell penetrating peptide and SP90 peptide. *Biomed. Pharmacother.* **2016**, *84*, 1783−1791.

(12) Ye, J.; Shin, M. C.; Liang, Q.; He, H.; Yang, V. C. 15 years of ATTEMPTS: a macromolecular drug delivery system based on the CPP-mediated intracellular drug delivery and antibody targeting. *J. Controlled Release* **2015**, *205*, 58−69.

(13) Park, H.; Tsutsumi, H.; Mihara, H. Cell-selective intracellular drug delivery using doxorubicin and alpha-helical peptides conjugated to gold nanoparticles. *Biomaterials* **2014**, *35*, 3480−3487.

(14) Figueira, T. N.; Augusto, M. T.; Rybkina, K.; Stelitano, D.; Noval, M. G.; Harder, O. E.; Veiga, A. S.; Huey, D.; Alabi, C. A.; Biswas, S.; Niewiesk, S.; Moscona, A.; Santos, N. C.; Castanho, M.; Porotto, M. Effective in vivo targeting of influenza virus through a cell-penetrating/fusion inhibitor tandem peptide anchored to plasma membrane. *Bioconjugate Chem.* **2018**, 3362−3376.

(15) Xiong, X. B.; Uludag, H.; Lavasanifar, A. Virus-mimetic polymeric micelles for targeted siRNA delivery. *Biomaterials* **2010**, *31*, 5886−5893.

(16) Boeneman, K.; Delehanty, J. B.; Blanco-Canosa, J. B.; Susumu, K.; Stewart, M. H.; Oh, E.; Huston, A. L.; Dawson, G.; Ingale, S.; Walters, R.; Domowicz, M.; Deschamps, J. R.; Algar, W. R.; Dimaggio, S.; Manono, J.; Spillmann, C. M.; Thompson, D.; Jennings, T. L.; Dawson, P. E.; Medintz, I. L. Selecting improved peptidyl motifs for cytosolic delivery of disparate protein and nanoparticle materials. *ACS Nano* **2013**, *7*, 3778−3796.

DOI: 10.1021/acsami.8b21027
ACS Appl. Mater. Interfaces 2019, 11, 2448−2458

(17) Dissanayake, S.; Denny, W. A.; Gamage, S.; Sarojini, V. Recent developments in anticancer drug delivery using cell penetrating and tumor targeting peptides. *J. Controlled Release* **2017**, *250*, 62−76.
(18) Zhu, L.; Kate, P.; Torchilin, V. P. Matrix metalloprotease 2-responsive multifunctional liposomal nanocarrier for enhanced tumor targeting. *ACS Nano* **2012**, *6*, 3491−3498.
(19) Buckel, L.; Savariar, E. N.; Crisp, J. L.; Jones, K. A.; Hicks, A. M.; Scanderbeg, D. J.; Nguyen, Q. T.; Sicklick, J. K.; Lowy, A. M.; Tsien, R. Y.; Advani, S. J. Tumor radiosensitization by monomethyl auristatin E: mechanism of action and targeted delivery. *Cancer Res.* **2015**, *75*, 1376−1387.
(20) Bolhassani, A. Potential efficacy of cell-penetrating peptides for nucleic acid and drug delivery in cancer. *Biochim. Biophys. Acta, Rev. Cancer* **2011**, *1816*, 232−246.
(21) Laakkonen, P.; Porkka, K.; Hoffman, J. A.; Ruoslahti, E. A tumor-homing peptide with a targeting specificity related to lymphatic vessels. *Nat. Med.* **2002**, *8*, 751−755.
(22) Ding, J.; Yao, J.; Xue, J.; Li, R.; Bao, B.; Jiang, L.; Zhu, J. J.; He, Z. Tumor-Homing Cell-Penetrating Peptide Linked to Colloidal Mesoporous Silica Encapsulated (-)-Epigallocatechin-3-gallate as Drug Delivery System for Breast Cancer Therapy in Vivo. *ACS Appl. Mater. Interfaces* **2015**, *7*, 18145−18155.
(23) Li, M.; Liu, P.; Gao, G.; Deng, J.; Pan, Z.; Wu, X.; Xie, G.; Yue, C.; Cho, C. H.; Ma, Y.; Cai, L. Smac therapeutic Peptide nanoparticles inducing apoptosis of cancer cells for combination chemotherapy with Doxorubicin. *ACS Appl. Mater. Interfaces* **2015**, *7*, 8005−8012.
(24) Xiong, X. B.; Lavasanifar, A. Traceable multifunctional micellar nanocarriers for cancer-targeted co-delivery of MDR-1 siRNA and doxorubicin. *ACS Nano* **2011**, *5*, 5202−5213.
(25) Shi, N. Q.; Qi, X. R. Taming the Wildness of "Trojan-Horse" Peptides by Charge-Guided Masking and Protease-Triggered Demasking for the Controlled Delivery of Antitumor Agents. *ACS Appl. Mater. Interfaces* **2017**, *9*, 10519−10529.
(26) Shi, N. Q.; Li, Y.; Zhang, Y.; Shen, N.; Qi, L.; Wang, S. R.; Qi, X. R. Intelligent "Peptide-Gathering Mechanical Arm" Tames Wild "Trojan-Horse" Peptides for the Controlled Delivery of Cancer Nanotherapeutics. *ACS Appl. Mater. Interfaces* **2017**, *9*, 41767−41781.
(27) Zhao, Y.; Ren, W.; Zhong, T.; Zhang, S.; Huang, D.; Guo, Y.; Yao, X.; Wang, C.; Zhang, W. Q.; Zhang, X.; Zhang, Q. Tumor-specific pH-responsive peptide-modified pH-sensitive liposomes containing doxorubicin for enhancing glioma targeting and anti-tumor activity. *J. Controlled Release* **2016**, *222*, 56−66.
(28) Cheng, H.; Zhu, J. Y.; Xu, X. D.; Qiu, W. X.; Lei, Q.; Han, K.; Cheng, Y. J.; Zhang, X. Z. Activable Cell-Penetrating Peptide Conjugated Prodrug for Tumor Targeted Drug Delivery. *ACS Appl. Mater. Interfaces* **2015**, *7*, 16061−16069.
(29) Yang, Y.; Yang, Y.; Xie, X.; Cai, X.; Zhang, H.; Gong, W.; Wang, Z.; Mei, X. PEGylated liposomes with NGR ligand and heat-activable cell-penetrating peptide-doxorubicin conjugate for tumor-specific therapy. *Biomaterials* **2014**, *35*, 4368−4381.
(30) Raemdonck, K.; De Smedt, S. C. Lessons in simplicity that should shape the future of drug delivery. *Nat. Biotechnol.* **2015**, *33*, 1026−1027.
(31) Molinaro, R.; Corbo, C.; Martinez, J. O.; Taraballi, F.; Evangelopoulos, M.; Minardi, S.; Yazdi, I. K.; Zhao, P.; De Rosa, E.; Sherman, M. B.; De Vita, A.; Toledano Furman, N. E.; Wang, X.; Parodi, A.; Tasciotti, E. Biomimetic proteolipid vesicles for targeting inflamed tissues. *Nat. Mater.* **2016**, *15*, 1037−1046.
(32) Polo, E.; Collado, M.; Pelaz, B.; Del Pino, P. Advances toward More Efficient Targeted Delivery of Nanoparticles in Vivo: Understanding Interactions between Nanoparticles and Cells. *ACS Nano* **2017**, *11*, 2397−2402.
(33) García-Alonso, S.; Ocana, A.; Pandiella, A. Resistance to Antibody-Drug Conjugates. *Cancer Res.* **2018**, *78*, 2159−2165.
(34) Yu, M.; Li, X.; Liang, R.; Yang, J.; Zhang, Y.; Wang, H. A new ligand of CD105 screened out by phage display technology provides a reliable identification of recurrent or metastasizing pleomorphic adenoma from pleomorphic adenoma. *Int. Immunopharmacol.* **2018**, *65*, 37−43.
(35) Ramsey, J. D.; Flynn, N. H. Cell-penetrating peptides transport therapeutics into cells. *Pharmacol. Ther.* **2015**, *154*, 78−86.
(36) Chen, L.; Zang, F.; Wu, H.; Li, J.; Xie, J.; Ma, M.; Gu, N.; Zhang, Y. Using PEGylated magnetic nanoparticles to describe the EPR effect in tumor for predicting therapeutic efficacy of micelle drugs. *Nanoscale* **2018**, *10*, 1788−1797.
(37) Maeda, H. Toward a full understanding of the EPR effect in primary and metastatic tumors as well as issues related to its heterogeneity. *Adv. Drug Delivery Rev.* **2015**, *91*, 3−6.
(38) Banks, W. A. From blood-brain barrier to blood-brain interface: new opportunities for CNS drug delivery. *Nat. Rev. Drug Discovery* **2016**, *15*, 275−292.
(39) Estrella, V.; Chen, T.; Lloyd, M.; Wojtkowiak, J.; Cornnell, H. H.; Ibrahim-Hashim, A.; Bailey, K.; Balagurunathan, Y.; Rothberg, J. M.; Sloane, B. F.; Johnson, J.; Gatenby, R. A.; Gillies, R. J. Acidity generated by the tumor microenvironment drives local invasion. *Cancer Res.* **2013**, *73*, 1524−1535.
(40) Flavell, R. R.; Truillet, C.; Regan, M. K.; Ganguly, T.; Blecha, J. E.; Kurhanewicz, J.; VanBrocklin, H. F.; Keshari, K. R.; Chang, C. J.; Evans, M. J.; Wilson, D. M. Caged [(18)F]FDG Glycosylamines for Imaging Acidic Tumor Microenvironments Using Positron Emission Tomography. *Bioconjugate Chem.* **2016**, *27*, 170−178.
(41) Li, P. P.; Nakanishi, A.; Shum, D.; Sun, P. C.; Salazar, A. M.; Fernandez, C. F.; Chan, S. W.; Kasamatsu, H. Simian virus 40 Vp1 DNA-binding domain is functionally separable from the overlapping nuclear localization signal and is required for effective virion formation and full viability. *J. Virol.* **2001**, *75*, 7321−7329.
(42) Liang, Y.; Li, S.; Wang, X.; Zhang, Y.; Sun, Y.; Wang, Y.; Wang, X.; He, B.; Dai, W.; Zhang, H.; Wang, X.; Zhang, Q. A comparative study of the antitumor efficacy of peptide-doxorubicin conjugates with different linkers. *J. Controlled Release* **2018**, *275*, 129−141.
(43) Allen, T. M.; Cullis, P. R. Liposomal drug delivery systems: from concept to clinical applications. *Adv. Drug Delivery Rev.* **2013**, *65*, 36−48.
(44) Hyun, H.; Park, J.; Willis, K.; Park, J. E.; Lyle, L. T.; Lee, W.; Yeo, Y. Surface modification of polymer nanoparticles with native albumin for enhancing drug delivery to solid tumors. *Biomaterials* **2018**, *180*, 206−224.
(45) Liu, Z.; Hu, B. H.; Messersmith, P. B. Convenient Synthesis of Acetonide Protected 3,4-Dihydroxyphenylalanine (DOPA) for Fmoc Solid-Phase Peptide Synthesis. *Tetrahedron Lett.* **2008**, *49*, 5519−5521.
(46) Dixon, M. J.; Bourre, L.; MacRobert, A. J.; Eggleston, I. M. Novel prodrug approach to photodynamic therapy: Fmoc solid-phase synthesis of a cell permeable peptide incorporating 5-aminolaevulinic acid. *Bioorg. Med. Chem. Lett.* **2007**, *17*, 4518−4522.
(47) Górnaś, P.; Misina, I.; Gravite, I.; Soliven, A.; Kaufmane, E.; Seglina, D. Tocochromanols composition in kernels recovered from different apricot varieties: RP-HPLC/FLD and RP-UPLC-ESI/MS(n) study. *Nat. Prod. Res.* **2015**, *29*, 1222−1227.
(48) Sanna, M.; Firinu, D.; Manconi, P. E.; Pisanu, M.; Murgia, G.; Piras, V.; Castagnola, M.; Messana, I.; del Giacco, S. R.; Cabras, T. The salivary proteome profile in patients affected by SAPHO syndrome characterized by a top-down RP-HPLC-ESI-MS platform. *Mol. Biosyst.* **2015**, *11*, 1552−1562.
(49) Janicka, M.; Kot-Wasik, A.; Paradziej-Lukowicz, J.; Sularz-Peszynska, G.; Bartoszek, A.; Namiesnik, J. LC-MS/MS Determination of Isoprostanes in Plasma Samples Collected from Mice Exposed to Doxorubicin or Tert-Butyl Hydroperoxide. *Int. J. Mol. Sci.* **2013**, *14*, 6157−6169.
(50) Zheng, J. S.; Yu, M.; Qi, Y. K.; Tang, S.; Shen, F.; Wang, Z. P.; Xiao, L.; Zhang, L.; Tian, C. L.; Liu, L. Expedient total synthesis of small to medium-sized membrane proteins via Fmoc chemistry. *J. Am. Chem. Soc.* **2014**, *136*, 3695−3704.
(51) Vermeulen, L. M. P.; Brans, T.; Samal, S. K.; Dubruel, P.; Demeester, J.; De Smedt, S. C.; Remaut, K.; Braeckmans, K. Endosomal Size and Membrane Leakiness Influence Proton

DOI: 10.1021/acsami.8b21027
ACS Appl. Mater. Interfaces 2019, 11, 2448−2458

Sponge-Based Rupture of Endosomal Vesicles. *ACS Nano* **2018**, *12*, 2332−2345.
(52) Maeda, H.; Nakamura, H.; Fang, J. The EPR effect for macromolecular drug delivery to solid tumors: Improvement of tumor uptake, lowering of systemic toxicity, and distinct tumor imaging in vivo. *Adv. Drug Delivery Rev.* **2013**, *65*, 71−79.

DOI: 10.1021/acsami.8b21027
ACS Appl. Mater. Interfaces 2019, 11, 2448−2458